Forward and inverse problem for cardiac magnetic field and electric potential using two boundary element methods*

Tang Fa-Kuan(唐发宽)[a)], Wang Qian(王 倩)[a)b)], Hua Ning(华 宁)[a)], Tang Xue-Zheng(唐雪正)[a)], Lu Hong(陆 宏)[a)], and Ma Ping(马 平)[b)†]

[a)] *Department of Cardiology, the 309th Hospital of PLA, Beijing* 100091, *China*

[b)] *Department of Physics, State Key Laboratory for Artificial Microstructure and Mesoscopic Physics, Peking University, Beijing* 100871, *China*

(Received 3 April 2010; revised manuscript received 4 August 2010)

This paper discusses the forward and inverse problem for cardiac magnetic fields and electric potentials. A torso-heart model established by boundary element method (BEM) is used for studying the distributions of cardiac magnetic fields and electric potentials. Because node-to-node and triangle-to-triangle BEM can lead to discrepant field distributions, their properties and influences are compared. Then based on constructed torso-heart model and supposed current source functional model—current dipole array, the magnetic and electric imaging by optimal constrained linear inverse method are applied at the same time. Through figure and reconstructing parameter comparison, though the magnetic current dipole array imaging possesses better reconstructing effect, however node-to-node BEM and triangle-to-triangle BEM make little difference to magnetic and electric imaging.

Keywords: cardiac magnetic imaging, cardiac electric imaging, boundary element method, torso-heart model

PACC: 0650, 8740, 8770

1. Background

The bioelectric sources in the heart region, together with electric currents driven by them in heart's surrounding areas will give rise to electric potentials on the body surface and magnetic fields outside the human body. These electric and magnetic signals can be recorded by electrocardiogram (ECG) and magnetocardiogram (MCG).[1,2] The ECG has been commonly accepted for diagnosing various heart diseases for decades, while the application of MCG is still immature because of the limitation of traditional MCG technology and capital, nevertheless electricity and magnetism are inseparably connected and they should be combined together to provide a more efficient and effective method of recognizing and testing heart diseases. Compared with widely used ECG, which is popular for its simplicity and cheapness, MCG also has several special advantages. As a kind of non-contacting and non-invasive detecting methods, MCG can offer high spatial resolution for magnetic signals, obtain direct-current magnetic fields due to the possible neglect of graded currents on skin, and record the magnitude alteration on a large scale considering the existence of ring currents. Since the discovery of high-temperature superconductor, the development of superconducting quantum interference device (SQUID) fabrication and SQUID magnetometer application have encouraged the MCG to be applied into highly sensitive biomagnetic measurement.[3−5]

Before clinic application and experiments in *vivo*, simulations of electric potentials and magnetic fields based on heart model is necessary because researchers should understand the structures and characteristics of electric potentials and magnetic fields in advance in order to guide the clinic and in *vivo* measurements. The boundary element method (BEM),[6,7] finite element method[8,9] and finite difference method,[10] etc. are usually used to construct heart and body models and determine the electric and magnetic distributions from a known current distribution. The BEM, being adopted in this paper to solve electric and magnetic

*Project supported by the State Key Development Program for Basic Research of China (Grant No. 2006CB601007), the National Natural Science Foundation of China (Grant No. 10674006), and the National High Technology Research and Development Program of China (Grant No. 2007AA03Z238).

†Corresponding author. E-mail: maping@pku.edu.cn

© 2010 Chinese Physical Society and IOP Publishing Ltd

forward problem, is a method to tessellate interfaces of different tissues and connect the electric potentials on interfaces with each other or with magnetic fields on measuring plane by transferring geometrical matrices.

Aiming at surveying heart electrophysiological activities, researchers also pay their attention to speculate cardiac current sources. This is an example of the inverse problem as opposed to the forward problem. Compared with transmission tomography and magnetic resonance imaging, which have higher resolution and provide anatomic images, magnetic and electric source imaging can give functional images though their resolution and accuracy are limited. The functional cardiac source can be chosen as one or more current dipoles or current multipole with undefined positions, magnitudes and orientations.[11−16] It also could be an array of current dipoles with fixed positions but unknown magnitudes and orientations, calculated by solving matrix-equation directly without iteration.[17−19] As to inverse algorithms for current dipole array imaging, many applicable algorithms have been raised in recent years, for example, the most original and classic—minimum-norm least squares method, the optimal weighted pseudo-inverse method and its special case—the optimal truncated pseudo-inverse method, L-curve method[20] and the truncated total least square method.[21] The optimal constrained linear inverse method[17] is selected to solve the inverse problem in this paper. One of the major themes of the paper is to reconstruct the functional current sources—current dipole array on account of simulated electric and magnetic data and discuss the influence of diverse BEM tessellating methods on the electric and magnetic imaging.

2. Method

2.1. Forward problem

As is known, the bioelectric currents inside the human heart will generate cardiac magnetic fields outside the body and electric potentials on the body surface, while these fields are caused not only by bioelectric currents, also called primary currents $\boldsymbol{J}^{\mathrm{p}}$ resulting from heart electrophysiological activities in conducting tissue, but by volume currents $\boldsymbol{J}^{\mathrm{v}}$ flowing passively to satisfy the continuity of currents. Let the total current $\boldsymbol{J} = \boldsymbol{J}^{\mathrm{p}} + \boldsymbol{J}^{\mathrm{v}}$ lie in a piecewise homogeneous volume conductor G, which consists of n homogeneous and isotropic parts G_j with closed surfaces S_j, $j = 1, 2, \ldots, n$, thus considering both $\boldsymbol{J}^{\mathrm{p}}$ and $\boldsymbol{J}^{\mathrm{v}}$, we can express the cardiac magnetic fields $\boldsymbol{B}(\boldsymbol{r})$ and cardiac electric potentials $V(\boldsymbol{r})$ on surface S_k as:[22]

$$\boldsymbol{B}(\boldsymbol{r}) = \boldsymbol{B}_0(\boldsymbol{r}) + \frac{\mu_0}{4\pi}\sum_{j=1}^{n}(\sigma_j' - \sigma_j'')\int_{S_j} V(\boldsymbol{r}')\frac{\boldsymbol{r}-\boldsymbol{r}'}{|\boldsymbol{r}-\boldsymbol{r}'|^3}\times \boldsymbol{n}_j \mathrm{d}S_j, \tag{1}$$

$$V(\boldsymbol{r}) = \frac{2\sigma_0}{(\sigma_k' + \sigma_k'')}V_0(\boldsymbol{r}) - \frac{1}{2\pi}\sum_{j=1}^{n}\frac{(\sigma_j' - \sigma_j'')}{(\sigma_k' + \sigma_k'')}\int_{S_j} V(\boldsymbol{r}')\frac{\boldsymbol{r}-\boldsymbol{r}'}{|\boldsymbol{r}-\boldsymbol{r}'|^3}\bullet \boldsymbol{n}_j \mathrm{d}S_j, \tag{2}$$

where

$$\boldsymbol{B}_0(\boldsymbol{r}) = \frac{\mu_0}{4\pi}\int_G \boldsymbol{J}^{\mathrm{p}}(\boldsymbol{r}')\times\frac{\boldsymbol{r}-\boldsymbol{r}'}{|\boldsymbol{r}-\boldsymbol{r}'|^3}\mathrm{d}v', \tag{3}$$

$$V_0(\boldsymbol{r}) = \frac{1}{4\pi\sigma_0}\int_G \boldsymbol{J}^{\mathrm{p}}(\boldsymbol{r}')\cdot\frac{\boldsymbol{r}-\boldsymbol{r}'}{|\boldsymbol{r}-\boldsymbol{r}'|^3}\mathrm{d}v' \tag{4}$$

are the magnetic induction and electric potential due to $\boldsymbol{J}^{\mathrm{p}}$ in an unbounded and homogeneous space respectively, μ_0 is the permeability in vacuum. σ_0 is the conductivity in the area containing current sources $\boldsymbol{J}^{\mathrm{p}}$. The $(\sigma_j' - \sigma_j'')V(\boldsymbol{r}')\boldsymbol{n}_j$ can be deemed as surface current density caused by the sudden change of conductivities on the interface S_j, $\boldsymbol{n}_j$ is the unit vector pointing to outside of $\mathrm{d}S_j$, σ_j' and σ_j'' are the conductivities on the inner and outer sides of S_j.

Simulated $\boldsymbol{B}(\boldsymbol{r})$ on measuring plane and $V(\boldsymbol{r})$ on body surface can be calculated according to Eqs. (1) and (2), which give an appropriate model of cardiac current sources, however, the second part on the right-hand side of these two equations is an integral, which is hard for computing directly. Only by tessellating S_j into tiny parts, these integral terms can be translated into summation and then computed analytically.

It is commonly accepted that S_j should be divided into many small triangles, while tessellating forms are diverse and here the method for division is chosen from the paper of Barr *et al.*[6] as shown in Fig. 1, where a torso-heart model is constructed by BEM. In this model, for simplification other tissues except for torso and heart are neglected, the areas inside the heart, and between heart surface S_{H} and torso surface S_{B} are thought to be homogeneous with conductivities σ_1 and σ_2, so $\boldsymbol{B}(\boldsymbol{r})$ and $V(\boldsymbol{r})$ expressions in this condition are

$$V_{\rm B}(\boldsymbol{r}) = \frac{2\sigma_1}{\sigma_2}V_{0,{\rm B}}(\boldsymbol{r}) + \frac{1}{2\pi}\frac{\sigma_1-\sigma_2}{\sigma_2}\int_{S_{\rm H}} V_{\rm H}(\boldsymbol{r}')\mathrm{d}\Omega_{\rm BH}(\boldsymbol{r},\boldsymbol{r}') + \frac{1}{2\pi}\int_{S_{\rm B}} V_{\rm B}(\boldsymbol{r}')\mathrm{d}\Omega_{\rm BB}(\boldsymbol{r},\boldsymbol{r}'), \quad (5)$$

$$V_{\rm H}(\boldsymbol{r}) = \frac{2\sigma_1}{\sigma_1+\sigma_2}V_{0,{\rm H}}(\boldsymbol{r}) + \frac{1}{2\pi}\frac{\sigma_1-\sigma_2}{\sigma_1+\sigma_2}\int_{S_{\rm H}} V_{\rm H}(\boldsymbol{r}')\mathrm{d}\Omega_{\rm HH}(\boldsymbol{r},\boldsymbol{r}') + \frac{1}{2\pi}\frac{\sigma_2}{\sigma_1+\sigma_2}\int_{S_{\rm B}} V_{\rm B}(\boldsymbol{r}')\mathrm{d}\Omega_{\rm HB}(\boldsymbol{r},\boldsymbol{r}'), \quad (6)$$

$$\boldsymbol{B}(\boldsymbol{r}) = \boldsymbol{B}_0(\boldsymbol{r}) + \frac{\mu_0}{4\pi}(\sigma_1-\sigma_2)\int_{S_{\rm H}} V_{\rm H}(\boldsymbol{r}')\frac{\boldsymbol{r}-\boldsymbol{r}'}{|\boldsymbol{r}-\boldsymbol{r}'|^3}\times\boldsymbol{n}_{\rm H}\mathrm{d}S_{\rm H} + \frac{\mu_0}{4\pi}\sigma_2\int_{S_{\rm B}} V_{\rm B}(\boldsymbol{r}')\frac{\boldsymbol{r}-\boldsymbol{r}'}{|\boldsymbol{r}-\boldsymbol{r}'|^3}\times\boldsymbol{n}_{\rm B}\mathrm{d}S_{\rm B}, \quad (7)$$

where

$$\mathrm{d}\Omega_{\rm ef}(\boldsymbol{r},\boldsymbol{r}') = \frac{\boldsymbol{r}'-\boldsymbol{r}}{|\boldsymbol{r}-\boldsymbol{r}'|^3}\cdot\boldsymbol{n}_f\mathrm{d}S_f$$

is an element of solid angle subtended at an observation point $\boldsymbol{r}$ on surface $S_{\rm e}$ by an area element $\mathrm{d}S_{\rm f}$ on surface $S_{\rm f}$, $\boldsymbol{r'}$ is the position of the element $\mathrm{d}S_{\rm f}$.

Integrals in Eqs. (5) and (6) can be rewritten in the form of summation. The electric potentials at discrete points on $S_{\rm B}$ and $S_{\rm H}$ are $V_{\rm B}$ and $V_{\rm H}$ respectively, $V_{\rm B} = (V_{\rm B}^1, V_{\rm B}^2, \ldots, V_{\rm B}^{N_{\rm BD}})^{\rm T}$, $V_{\rm H} = (V_{\rm H}^1, V_{\rm H}^2, \ldots, V_{\rm H}^{N_{\rm HD}})^{\rm T}$, $N_{\rm BD}$ and $N_{\rm HD}$ are the numbers of discrete points on $S_{\rm B}$ and $S_{\rm H}$. From rewritten Eqs. (5) and (6) with summation form, it is found that $V_{\rm B}$ and $V_{\rm H}$ are connected to their corresponding electric potentials $V_{0,{\rm B}} = (V_{0,{\rm B}}^1, V_{0,{\rm B}}^2, \ldots, V_{0,{\rm B}}^{N_{\rm DB}})^{\rm T}$, and $V_{0,{\rm H}} = (V_{0,{\rm H}}^1, V_{0,{\rm H}}^2, \ldots, V_{0,{\rm H}}^{N_{\rm DH}})^{\rm T}$ in an unbounded space by a P matrix only related to the shapes of $S_{\rm B}$ and $S_{\rm H}$, and their geometrical relationship reads

$$\begin{pmatrix} P_{\rm BB} & P_{\rm BH} \\ P_{\rm HB} & P_{\rm HH} \end{pmatrix}\begin{pmatrix} V_{\rm B} \\ V_{\rm H} \end{pmatrix} = -\begin{pmatrix} \dfrac{2\sigma_1}{\sigma_2}V_{0,{\rm B}} \\ \dfrac{2\sigma_1}{\sigma_1+\sigma_2}V_{0,{\rm H}} \end{pmatrix}. \quad (8)$$

The $V_{0,{\rm B}}$ and $V_{0,{\rm H}}$ have precise analytical expressions, so given a functional source model, they can be calculated easily. According to Eq. (8), through finding the inverse of matrix P we can obtain $V_{\rm B}$ and $V_{\rm H}$.

Next, the perpendicular component of $\boldsymbol{B}(\boldsymbol{r})$ at measuring point $\boldsymbol{r}^i$ with discrete form is

$$\begin{aligned} B^i(\boldsymbol{r}) = {} & B_0^i(\boldsymbol{r}) + \frac{\mu_0}{4\pi}\sigma_2\sum_{j=1}^{N_{\rm BT}}\Phi_{\rm B}^j\frac{\boldsymbol{r}^i-\boldsymbol{r}_{\rm B}^{j'}}{\left|\boldsymbol{r}^i-\boldsymbol{r}_{\rm B}^{j'}\right|^3} \\ & \times\boldsymbol{n}_{\rm B}^j\cdot\boldsymbol{e}^i\Delta S_{\rm B}^j \\ & + \frac{\mu_0}{4\pi}(\sigma_1-\sigma_2)\sum_{j=1}^{N_{\rm HT}}\Phi_{\rm H}^j\frac{\boldsymbol{r}^i-\boldsymbol{r}_{\rm H}^{j'}}{\left|\boldsymbol{r}^i-\boldsymbol{r}_{\rm H}^{j'}\right|^3} \\ & \times\boldsymbol{n}_{\rm H}^j\cdot\boldsymbol{e}^i\Delta S_{\rm H}^j, \end{aligned} \quad (9)$$

where $N_{\rm BT}$ and $N_{\rm HT}$ are triangle numbers on surfaces $S_{\rm B}$ and $S_{\rm H}$ respectively, $\Phi_{\rm B}^j$ and $\Phi_{\rm H}^j$ are chosen to be the mean potential of the three apex-potential of the triangle $\Delta S_{\rm B}^j$ and $\Delta S_{\rm H}^j$ respectively, $\Phi_{\rm B} = (\Phi_{\rm B}^1, \Phi_{\rm B}^2, \ldots, \Phi_{\rm B}^{N_{\rm BT}})^{\rm T}$, $\Phi_{\rm H} = (\Phi_{\rm H}^1, \Phi_{\rm H}^2, \ldots, \Phi_{\rm H}^{N_{\rm HT}})^{\rm T}$.

Two methods for BEM tessellation are mainly discussed in this article. One is node-to-node tessellation, and the other is triangle-to-triangle tessellation. As to the first tessellating method, where $N_{\rm BD}$ and $N_{\rm HD}$ are chosen to be the number of the discrete nodes on $S_{\rm B}$ and $S_{\rm H}$:$N_{\rm B}$ and $N_{\rm H}$, thus the P matrix ($(N_{\rm B}+N_{\rm H})\times(N_{\rm B}+N_{\rm H})$ dimension) consists of coefficients (elements of solid angle) for the nodes. When it comes to the second tessellating method, where scattered points are the centroids of the triangles and potentials are taken constant over each triangle, the potentials can be solved from Eqs. (5) and (6), where the matrix P ($(N_{\rm BT}+N_{\rm HT})\times(N_{\rm BT}+N_{\rm HT})$ dimension) contains the solid angles subtended at the centre of each triangle by all other triangles. To distinguish potentials in these two tessellations, potentials on nodes are expressed by $V_{\rm B}$ and $V_{\rm H}$, and potentials at the centre of each triangle are set to be $\Phi_{\rm B}$ and $\Phi_{\rm H}$.

2.2. Inverse problem

The magnetic field detected by magnetometer or magnetogradiometer at point $\boldsymbol{r}^i$ and the electric potential measured with point electrode at point $\boldsymbol{r}^k$ on torso surface can be written in the form as follows:[23]

$$\begin{aligned} & B^i = B_0^i + \sum_{m=1}^{N_{\rm BD}} A_{\rm B}^{im}V_{0,{\rm B}}^m + \sum_{n=1}^{N_{\rm HD}} A_{\rm H}^{in}V_{0,{\rm H}}^n, \\ & i = 1, 2\ldots, M, \end{aligned} \quad (10)$$

$$\begin{aligned} & V^k = \sum_{m=1}^{N_{\rm BD}} C_{\rm B}^{km}V_{0,{\rm B}}^m + \sum_{n=1}^{N_{\rm HD}} C_{\rm H}^{kn}V_{0,{\rm H}}^n, \\ & k = 1, 2\ldots, N_{\rm BD}, \end{aligned} \quad (11)$$

where the matrices $A_{\rm B}$ ($M\times N_{\rm BD}$), $A_{\rm H}$ ($M\times N_{\rm HD}$), $C_{\rm B}$ ($N_{\rm BD}\times N_{\rm BD}$) and $C_{\rm H}$ ($N_{\rm BD}\times N_{\rm HD}$) consist of geometrical factors and are computed only once unless the geometry or the detector configuration is altered. In this computation, discretisation points are the centroids of the triangles on $S_{\rm B}$ and $S_{\rm H}$, so $A_{\rm B}$, $A_{\rm H}$, $C_{\rm B}$ and $C_{\rm H}$ will have different expressions in node-to-node and triangle-to-triangle tessellations.

Furthermore, the magnetic field and the electric potential are the linear function of the primary current

distribution:

$$B^i = \int_G \boldsymbol{L}^i(\boldsymbol{r}') \cdot \boldsymbol{J}^{\mathrm{p}}(\boldsymbol{r}')\mathrm{d}^3 r', \tag{12}$$

$$V^k = \int_G \boldsymbol{L}^k_{\mathrm{E}}(\boldsymbol{r}') \cdot \boldsymbol{J}^{\mathrm{p}}(\boldsymbol{r}')\mathrm{d}^3 r', \tag{13}$$

where coefficients $\boldsymbol{L}^i(\boldsymbol{r}')$ and $\boldsymbol{L}^k_{\mathrm{E}}(\boldsymbol{r}')$ are called as lead field of a magnetometer at $\boldsymbol{r}^i$ and electric lead field of an electrode at $\boldsymbol{r}^k$ respectively. They are only concerned with source, observation point distributions and model geometries.

Comparing discrete Eqs. (5) and (7) with Eqs. (12) and (13), we can obtain

$$\begin{aligned}\boldsymbol{L}^i(\boldsymbol{r}') = {} & \boldsymbol{L}^i_0(\boldsymbol{r}') + \sum_{m=1}^{N_{\mathrm{BT}}} A^{im}_{\mathrm{B}} \boldsymbol{L}^m_{0,\mathrm{E}}(\boldsymbol{r}') \\ & + \sum_{n=1}^{N_{\mathrm{HT}}} A^{in}_{\mathrm{H}} \boldsymbol{L}^n_{0,\mathrm{B}}(\boldsymbol{r}'),\end{aligned} \tag{14}$$

$$\boldsymbol{L}^k_{\mathrm{E}}(\boldsymbol{r}') = \sum_{m=1}^{N_{\mathrm{BT}}} C^{im}_{\mathrm{B}} \boldsymbol{L}^m_{0,\mathrm{E}}(\boldsymbol{r}') + \sum_{n=1}^{N_{\mathrm{HT}}} C^{in}_{\mathrm{H}} \boldsymbol{L}^n_{0,\mathrm{E}}(\boldsymbol{r}'), \tag{15}$$

where

$$\boldsymbol{L}^i_0(\boldsymbol{r}') = \frac{\mu_0}{4\pi} \frac{(\boldsymbol{r}^i - \boldsymbol{r}') \times \boldsymbol{e}^i}{|\boldsymbol{r}^i - \boldsymbol{r}'|^3},$$

$$\boldsymbol{L}^k_{0,\mathrm{E}}(\boldsymbol{r}') = \frac{1}{4\pi\sigma} \frac{\boldsymbol{r}^k - \boldsymbol{r}'}{|\boldsymbol{r}^k - \boldsymbol{r}'|^3}$$

are lead field and electric lead field without consideration of boundary effect respectively.

The goal of inverse problem is to reconstruct the primary current distribution, while we cannot acquire the analytical solutions from Eqs. (12) and (13) because of the integration terms and they should be discretized by supposing that the primary currents are distributed on a thin layer with thickness h, parallel to the magnetic observation plane, and tessellated evenly into N cells, thus equations (12) and (13) can be modified in a summation form:

$$B^i = \sum_{j=1}^{N} \boldsymbol{L}^i(\boldsymbol{r}') \cdot \boldsymbol{J}(\boldsymbol{r}') h \Delta S^{j'},$$
$$i = 1, 2, \ldots, M_{\mathrm{B}}, \tag{16}$$

$$V^k = \sum_{j=1}^{N} \boldsymbol{L}^k_{\mathrm{E}}(\boldsymbol{r}') \cdot \boldsymbol{J}(\boldsymbol{r}') h \Delta S^{j'},$$
$$k = 1, 2, \ldots, M_{\mathrm{V}}, \tag{17}$$

where $\boldsymbol{J}(\boldsymbol{r}')h\Delta S^{j'}$ with dimension of A · m could be deemed as a current dipole $\boldsymbol{Q}^j = (Q^j_x, Q^j_y, Q^j_z)^{\mathrm{T}}$. In each cell of the thin layer, there will be a current dipole, composing current dipole array as the equivalent current sources.

According to Eqs. (16) and (17), $B = (B^1, B^2, \ldots, B^{M_{\mathrm{B}}})^{\mathrm{T}}$, $V = (V^1, V^2, \ldots, V^{M_v})^{\mathrm{T}}$, $Q = (\boldsymbol{Q}^1, \boldsymbol{Q}^2, \ldots, \boldsymbol{Q}^N)^{\mathrm{T}}$ satisfy

$$B = LQ, \tag{18}$$

$$V = L_{\mathrm{E}}Q, \tag{19}$$

where L ($M_{\mathrm{B}} \times N$) and L_{E} ($M_{\mathrm{V}} \times N$) are lead field matrix and electric lead field matrix.

Obviously, it is easy to assume that given L^{-1} and L^{-1}_{E}, the solution Q for cardiac magnetic and electric inverse problems are obtained. However, under most circumstances, because of the ill-posed problem on calculating the inverse of matrices L and L_{E}, the solution Q does not exist or is indefinite. Even so, we are still able to get the most optimally approximate solution $\hat{Q}$, which minimizes the residual $\Delta^2 = \|B - L\hat{Q}\|^2$ and norm $\|\hat{Q}\|^2$. The OCLIM[17] is chosen to solve the inverse problem here to satisfy matrix equation:

$$\hat{Q} = HB. \tag{20}$$

For more realistic case, the measurement noises can be added to magnetic fields and electric potentials:

$$B = LQ + W_{\mathrm{B}}, \tag{21}$$

$$V = L_{\mathrm{E}}Q + W_{\mathrm{V}}, \tag{22}$$

where W_{B} and W_{V} are noise vectors $W_{\mathrm{B}} = (W^1_{\mathrm{B}}, W^2_{\mathrm{B}}, \ldots, W^{M_{\mathrm{B}}}_{\mathrm{B}})^{\mathrm{T}}$, $W_{\mathrm{V}} = (W^1_{\mathrm{V}}, W^2_{\mathrm{V}}, \ldots, W^{M_{\mathrm{V}}}_{\mathrm{V}})^{\mathrm{T}}$.

In the system represented by Eqs. (21) and (22), the OCLIM estimator for source reconstruction $H = L^+$ has the expression:

$$H = (AL^{\mathrm{T}} + \Gamma)(LAL^{\mathrm{T}} + L\Gamma + \Gamma^{\mathrm{T}}L^{\mathrm{T}} + \Sigma)^{-1}. \tag{23}$$

where covariance matrices $A = EQQ^{\mathrm{T}}$ and $\Sigma = EWW^{\mathrm{T}}$, cross-covariance between the source and noise amplitude vectors is $\Gamma = EQW^{\mathrm{T}}$.

2.3. Evaluation of the inverse solution

In order to evaluate the reconstruction effect, we put forward the residual χ^2 and its mean value $E\chi^2$, which denote how closely reconstructed field values match the measured signals and how closely a reconstruction and the given measurements match on average,

$$\begin{aligned}\chi^2 = {} & (B - L\hat{Q})^{\mathrm{T}} \Sigma^{-1} (B - L\hat{Q}) \\ = {} & B^{\mathrm{T}}(I - LH)^{\mathrm{T}} \Sigma^{-1} (I - LH) B,\end{aligned} \tag{24}$$

$$E\chi^2 = EB^{\mathrm{T}}(I - LH)^{\mathrm{T}} \Sigma^{-1} (I - LH) B. \tag{25}$$

3. Numerical simulation

3.1. Torso-heart model and current dipole array

As is shown in Fig. 1, a torso-heart model is constructed, where the torso is set to be an ellipsoid ($x^2/a^2+y^2/b^2+z^2/c^2=1$) with its structural parameters a, b, c chosen corresponding to the realistic torso's size and the simulated heart is simplified as a sphere with radius r. To simulate magnetic and electric distributions analytically, the torso and heart surface are tessellated by node-to-node BEM and triangle-to-triangle BEM whose methods are mentioned in Subsection 2.1.

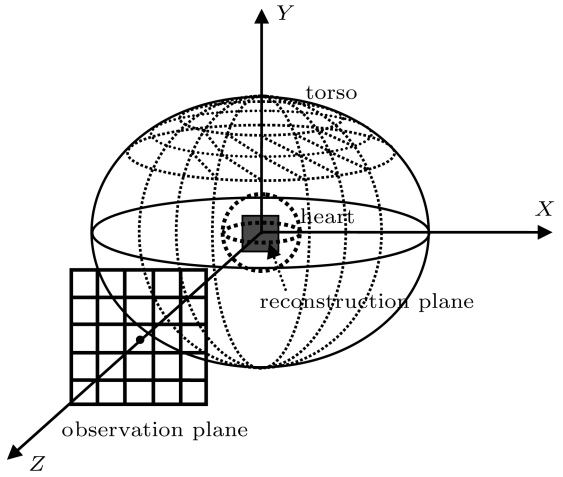


Fig. 1. Torso-heart model constructed by BEM. The observation plane is placed in front of the model. The reconstruction plane sits in the centre of heart model. Dash lines along the longitude and latitude show how this model is tessellated.

Part of the torso with $z>0$ is treated as the front side of human. In front of the torso-heart model there lays a magnetic measuring plane which is parallel to XOY plane and next to torso's front side. Nodes on this plane are N ($N=n\times n$) measuring points.

The square area in the centre of heart in Fig. 1 is the reconstruction plane with M ($M=m\times m$) reconstructing points, coinciding with XOY plane. Cardiac primary currents are supposed to distribute on this plane. The source model of current dipole array presumes a set of current dipoles distributed homogeneously on the reconstruction plane, that is to say, each grid centre places one dipole, thus all the dipoles' positions are fixed. This priori serves as a necessary condition for inverse computation described here because only when all the dipoles' positions are defined, the magnetic fields and electric potentials can have linear relationship with current sources.

The testing source for generating magnetic fields and electric potentials is chosen to be a single current dipole $\boldsymbol{p}$, which is a proper functional source model for imitating cardiac electrophysiological activities during QRS and ST-T complex in one cardiac cycle, where magnetic and electric magnitude are much larger than that in other moment in one cardiac cycle, in other words, the signal-to-noise ratio (SNR) is much larger, thus it is easier for researchers to pick up useful biological information from these periods. As a result, QRS and ST-T complex containing quite valuable ECG and MCG information has been exploited by most doctors to diagnose heart related diseases.

3.2. Comparison of node-to-node BEM and triangle-to-triangle BEM

In this section, based on the torso-heart model and BEM, the influence of two different BEM tessellating methods on the magnetic field distribution is discussed. The model structural parameters are the same for two tessellating methods: as to ellipsoidal torso $a=b=0.2$ m, $c=0.1$ m, as to spherical heart $r=0.05$ m. The conductivities of heart muscle and inner torso tissue are 0.10 S/m and 0.04 S/m, respectively.[24] For BEM, 24 areas are divided evenly along the latitude and longitude of torso and heart surface, producing 554 nodes and 1104 triangles on both surfaces. The test current dipole $\boldsymbol{p}=(-10^{-6},10^{-6},10^{-6})$ A $\cdot$ m is placed at $\boldsymbol{r}_0=(0,0,0)$ m. The observation plane is 0.02 m in front of the torso.

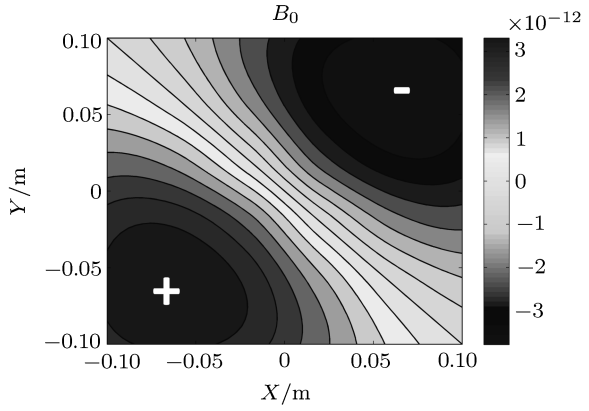


Fig. 2. The MCG map for magnetic fields in an unbounded space B_0.

As for diverse tessellations, in unbounded space the magnetic fields B_0 are the same, while in node-to-node BEM model constructed according to Ref. [6] and triangle-to-triangle BEM model described similarly with Ref. [25], the magnetic fields B in bounded space are different. Figure 2 shows the MCG map of B_0 on the observation plane, '+' denotes the positive magnetic area and '–' signifies the negative magnetic area.

Considering the boundary effect, we shall modify B_0 by volume magnetic fields B_V produced by surface currents. Although two kinds of modifications caused by diverse BEM tessellations are roughly the same, magnitudes of magnetic fields B with boundary have a slight difference at the same measuring point, leading to discrepancies on the shape of the MCG map of B shown by Fig. 3. Figures 3(a) and 3(c) are B's MCG maps with node-to-node tessellation and triangle-to-triangle tessellation, respectively. The magnitudes of magnetic fields in the bounded space are about 1/3 of those in the unbounded space, which means B_0 is counteracted partly by B_V. Figures 3(b) and 3(d) are the MCG maps of volume magnetic fields B_V. From these four comparing pictures, we can have a better understanding of how and in what degree does B_V offset B_0, the impact of different BEM tessellating methods on the magnitudes of B and get prepared for magnetic and electric imaging based on distinct BEM tessellations.

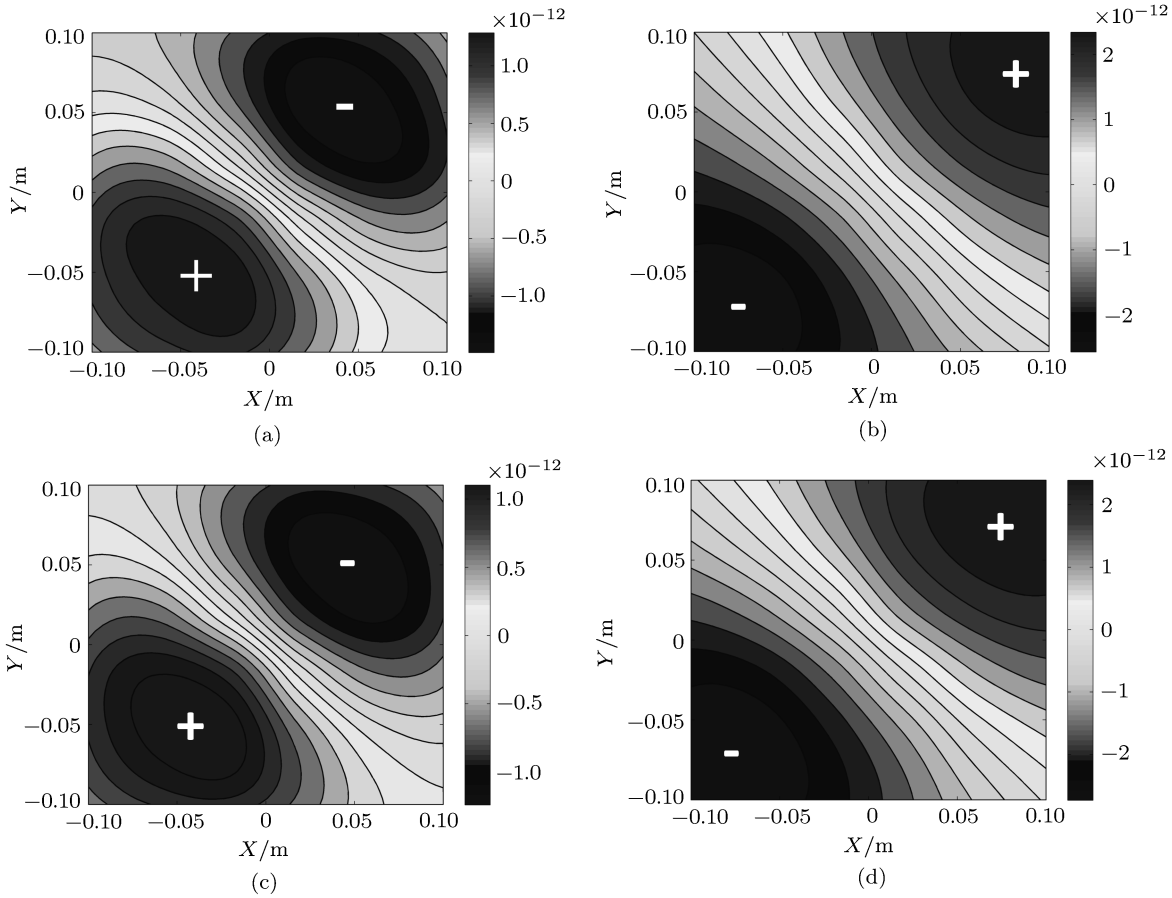


Fig. 3. Comparing figures of B and B_V simulated by node-to-node BEM and triangle-to-triangle BEM. (a) and (c) are B's distributions with node-to-node and triangle-to-triangle tessellation, respectively. (b) and (d) reveal B_V's distributions with node-to-node and triangle-to-triangle tessellation, separately.

The current dipole array reconstruction using these two tessellating methods will be discussed in the next section, where the magnetic and electric imagings are both considered and compared.

3.3. Current dipole array reconstruction

The goal of this part is to conclude the impact of diverse BEM tessellations on the electric and magnetic imaging using OCLIM. The torso-heart shape parameters are the same as before. Current dipoles serving as cardiac electric sources are assumed to distribute evenly on a thin layer at the centre of the heart, the nearest distance between the two would-be reconstructed dipoles is 0.005 m, and there are 14×14 dipoles in all. A single current dipole placed at $(0, 0, 0)$ with its magnitude $(-10^{-6}, 10^{-6}, 10^{-6})$ A $\cdot$ m is assumed to be the testing source for producing simulated fields. As to inputs for inverse computation, the simulated magnetic fields are

obtained from 6×6 measuring grids, the electric potentials come from all the nodes or centroids of tessellated triangles.

Let us suppose that the magnetic and electric imagings are applied without measuring noises originally, thus under this condition current dipole array reconstructions considering two BEM tessellations are shown in Fig. 4. Figures 4(a) and 4(b) are current dipole array reconstructions resting on magnetic fields with node-to-node and triangle-to-triangle BEM tessellations respectively. Figures 4(c) and 4(d) manifest the electric reconstructions of current dipole array with node-to-node and triangle-to-triangle BEM tessellations respectively. Through comparison, the effect of magnetic imaging is better than that of electric imaging clearly. At the same time, the imaging depending on node-to-node BEM embraces more favourable effect than imaging based on triangle-to-triangle BEM.

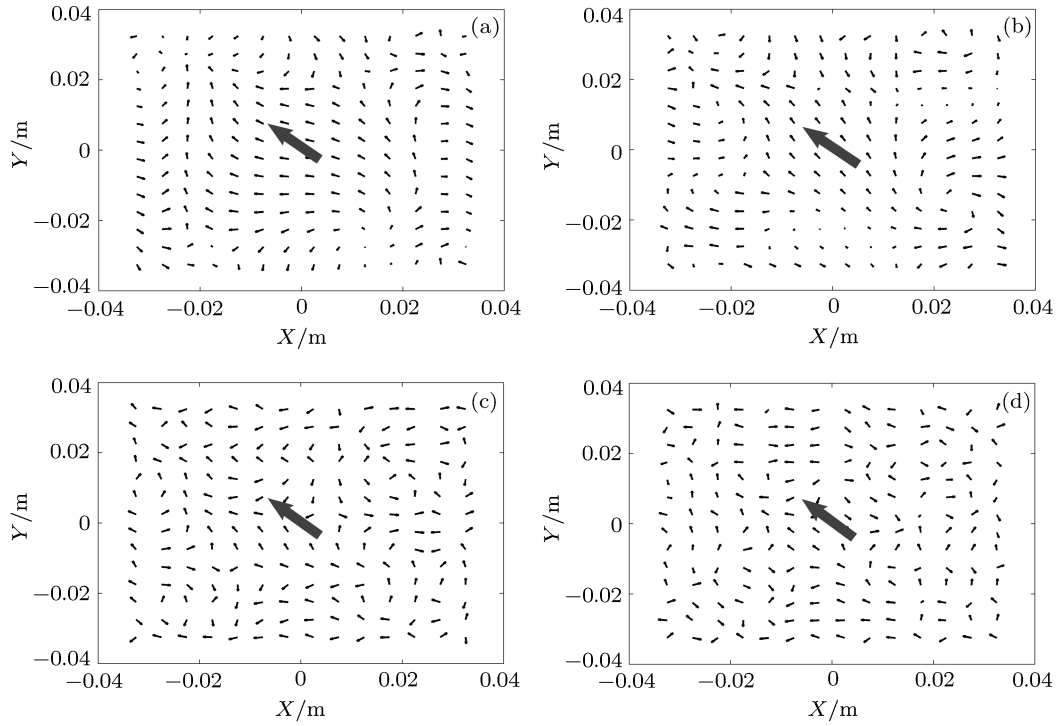


Fig. 4. Magnetic and electric dipole reconstructions without noises during considering two BEM tessellating methods. (a) and (b) are magnetic dipole reconstruction with node-to-node tessellation and triangle-to-triangle tessellation, respectively. (c) and (d) display electric dipole reconstruction resting on node-to-node tessellation and triangle-to-triangle tessellation, separately.

Next, the impact of noises on current dipole reconstruction will be discussed. Though there exist various kinds of noises in the procedure of measurements, only the commonly emerged random noises are regarded here. Once these noises are added to the simulated magnetic fields and electric potentials, the imaging effect, especially the dipole symmetry and direction consistence with testing source will be influenced without any doubt, which is obvious in Fig. 5 where the SNR is about 57 dB. The arrangement of four reconstruction pictures is the same as those in Fig. 4. First, as to Figs. 5(a) and 5(b), the magnetic reconstruction with triangle-to-triangle BEM tessellation is more severely influenced by random noises. Dipoles in central part of Fig. 5(b) are forced to change their directions in high degree even though they have the tendency to have the similar direction with the testing dipole. Secondly, from Figs. 5(c) and 5(d), dipole array's direction consistence with testing dipole is poor. In particular, the z components of current dipoles have increased greatly according to Fig. 5(d). The weak electric reconstructing effect could be partly attributed to the complexity of its inputs.

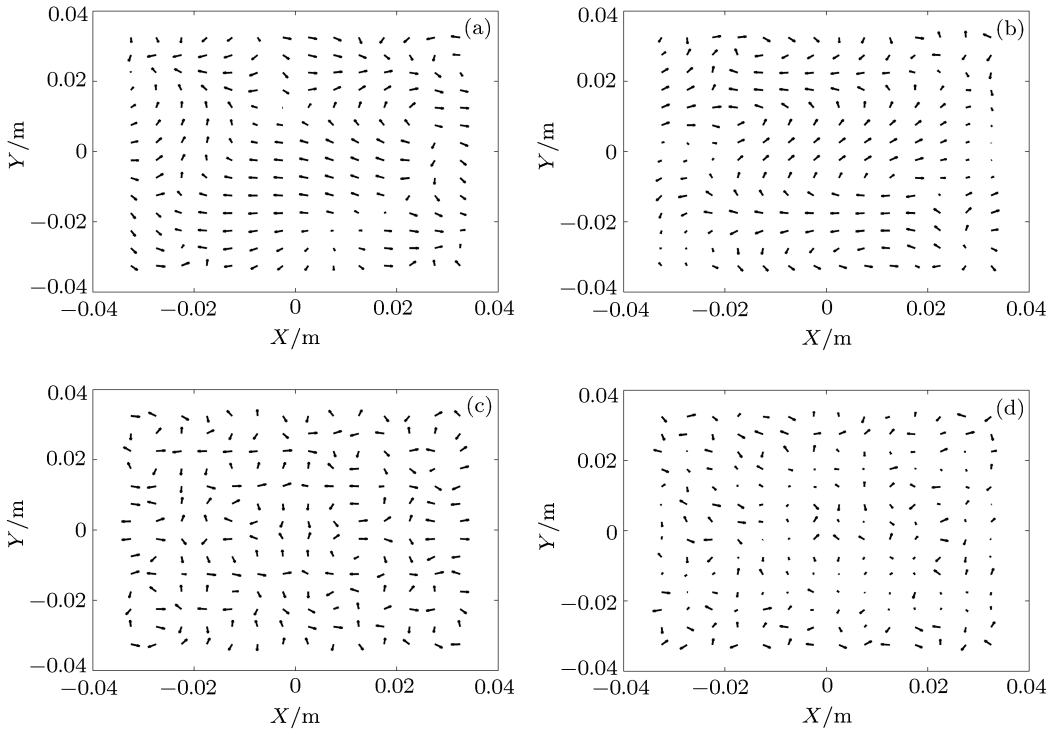


Fig. 5. Magnetic and electric dipole reconstructions with random noises (SNR ≈ 57 dB) during considering two BEM tessellating methods. (a) and (b) show magnetic dipole reconstruction with node-to-node tessellation and triangle-to-triangle tessellation, respectively. (c) and (d) are electric dipole reconstruction with node-to-node tessellation and triangle-to-triangle tessellation, respectively.

In order to describe the reconstructing effect quantitatively, two imaging parameters are brought forward: residual χ^2, which represents how closely the measured and reconstructed field values match; mean residual $E\chi^2$, which reveals how closely a reconstruction matches the given measurements on average. Figure 6 shows residual χ^2 as the function of SNR, line with marker '$*$' expresses the residual of magnetic imaging using node-to-node BEM and its nearest '$\circ$' line is the tendency of magnetic imaging residual based on triangle-to-triangle BEM. As for electric imaging, lines with marker '$+$' and '$\times$' are residuals as the function of SNR adopting node-to-node and triangle-to-triangle BEM tessellating methods respectively. Note that Y axis adopts χ^2's denary logarithm, $\log_{10}\chi^2$. The common property of these four lines is that they change gently before 50 dB, though '$\times$' line's flat tendency lasts longer to about 80 dB. After that, four lines are all increasing with SNR's augmentation. The differences among these lines focus on their values of $\log_{10}\chi^2$. The '$*$' and '$\circ$' lines' magnitudes are close and much smaller than '$+$' and '$\times$' lines' magnitudes, which are relatively distant from each other. This phenomenon demonstrates that the magnetic reconstructing effect is better than electric reconstructing effect with regard to OCLIM.

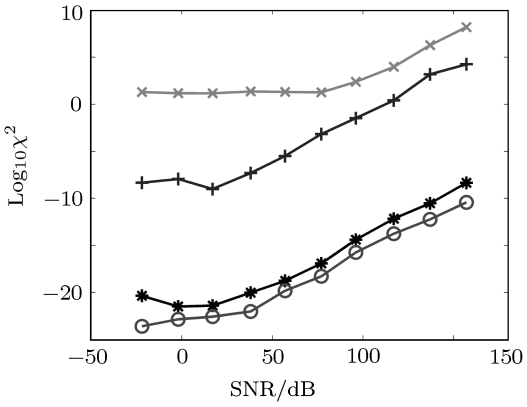


Fig. 6. Residual as the function of SNR. Lines with the marker '$*$' and '$\circ$' present the residual of magnetic imaging using node-to-node and triangle-to-triangle BEM; '$+$' and '$\times$' lines denote electric imaging residual with node-to-node and triangle-to-triangle BEM respectively. The $\log_{10}\chi^2$ serves as the scale of Y axis.

Figure 7 displays mean residual $E\chi^2$ as the function of SNR, where the meanings of markers '$*$', '$\circ$', '$+$', '$\times$' are identical with those meanings in Fig. 6. The Y axis here also adopts χ^2's denary logarithm, $\log_{10}\chi^2$. Four $E\chi^2$ lines are very close to each other and decrease linearly since 0 dB as shown in Fig. 7(a)

and for clearness these lines are magnified at a short SNR spanned from about 70 dB to 85 dB in Fig. 7(b).

After examining reconstruction parameters χ^2 and $E\chi^2$, we conclude that the OCLIM is a more appropriate method for magnetic inverse problem, meanwhile the differences of imaging effects between diverse BEM tessellations are not obvious. The poor electric imaging effect may result from the large amount of chosen measuring points and the inverse algorithm. Our following work will focus on how to choose the electric potential distribution as inputs and what inverse algorithm is more proper for electric imaging.

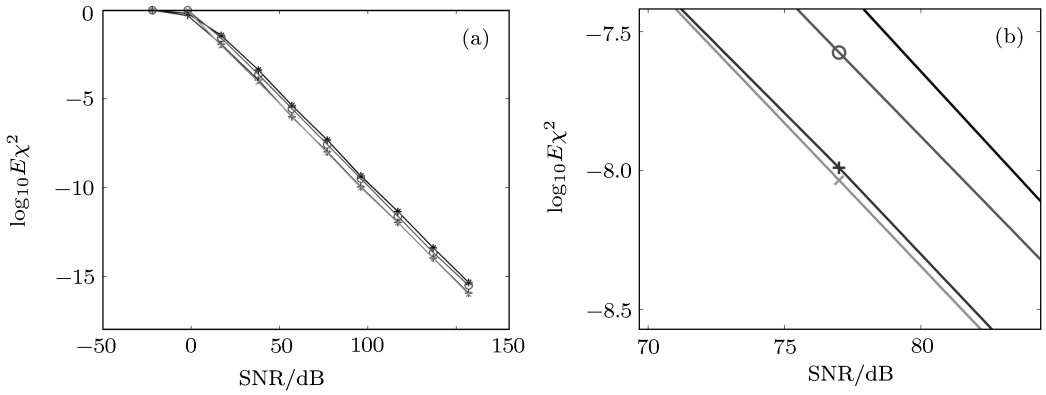


Fig. 7. Mean residual as the function of SNR. For clearness, picture (b) is the magnified type of picture (a) in smaller period of SNR. The meanings of diverse markers '∗', '○', '+', '×' are identical with those meanings in Fig. 6.

4. Conclusion

This paper mainly discusses the magnetic and electric forward and inverse problems. As far as the forward problem is concerned, a torso-heart model is constructed by BEM, where the torso and heart surfaces are tessellated by node-to-node and triangle-to-triangle BEM. Depending on single current dipole as testing source for generating simulating fields, the cardiac magnetic fields outside human torso considering boundary effect are obtained and compared. As for diverse BEM tessellations, the MCG map's shapes are roughly the same, though the magnitudes at the identical measuring points are relatively discrepant. Exploiting imitated magnetic and electric data from current dipole as inputs, we also realize the magnetic and electric imaging resting on models established by node-to-node and triangle-to-triangle tessellations. Figures of current dipole array reconstruction with and without random noises are given, and then two parameters χ^2 and $E\chi^2$ denoting imaging effects are calculated and their changing tendencies as the function of SNR are shown. From the comparison of four kinds of inverse computation using OCLIM, the magnetic imaging has better reconstructing effect when the current dipole array is used as functional cardiac current source model. However, diverse tessellating methods make little difference to reconstructing effect. The magnetic and electric forward and inverse problems help us decide the realistic measuring areas in *vivo* and clinic measurements to understand the cardiac activities functionally and explore a combined detecting method with ECG and MCG.

References

[1] Ma P, Yao K, Xie F X, Zhang S Y, Deng P, He D F, Zhang F, Liu L Y, Nie R J, Wang F R, Wang S Z and Dai Y D 2002 *Acta Phys. Sin.* **51** 224 (in Chinese)

[2] Gao J, Yang T, Ma P and Dai Y D 2010 *Chin. Phys.* B **19** 067402

[3] Ma P, Liu L Y, Zhang S Y, Wang X, Xie F X, Deng P, Nie R J, Wang S Z, Dai Y D and Wang F R 2002 *Acta Phys. Sin.* **51** 406 (in Chinese)

[4] Koch H 2001 *IEEE Trans. Appl. Supercond.* **11** 49

[5] Sternickel K and Braginski A I 2006 *Supercond. Sci. Technol.* **19** S160

[6] Barr R C, Ramsey M and Spach M S 1977 *IEEE Trans. Biom. Eng.* **24** 1

[7] Horacek B M and Clements 1997 *Math. Biosci.* **144** 119

[8] Johnson C R 1997 *Crit. Rev. Biomed. Eng.* **25** 1

[9] Gullmar D, Reichenbach J R, Anwander A, Knosche T, Wolters C H, Eiselt M and Haueisen J 2005 *Int. J. Bioelectromag.* **7** 108

[10] Lemieux L, McBride A and Hand J W 1996 *Phys. Med. Biol.* **41** 1079

[11] Arthur R M and Geselowitz D B 1970 *IEEE Trans. Biomed. Eng.* **17** 141

[12] Cuffin B N and Cohen D 1977 *IEEE Trans. Biomed. Eng.* **24** 372

[13] Lutkenhoner, Lehnertz B K, Hoke M and Pantev C 1991 *Acta OtoLaryngol* **491** 94

[14] Jerbi K, Mosher J C, Baillet S and Leahy R M 2002 *Phys. Med. Biol.* **47** 523

[15] Koch H and Haberkorn W 2001 *Phil. Trans. R. Soc. Lond.* **359** 1287

[16] Nenonen J, Katila T, Leinio M, Montonen J, Makijarvi M and Siltanen P 1991 *IEEE Trans. Biomed. Eng.* **38** 648

[17] Hughett P 1995 *Annals Biom. Eng.* **23** 506

[18] Wang J Z, Williamson S J and Kaufaman L 1992 *IEEE Trans. Biomed. Eng.* **39** 665

[19] Wang J Z 1993 *IEEE Trans. Biomed. Eng.* **40** 387

[20] Shou G F, Xia L, Jiang M F, Liu F and Crozier S 2008 *IEEE Trans. Biomed. Eng.* **55** 1327

[21] Horacek B M, Purcell C, Lamothe R, Leon L J and Merritt R 1987 *Phys. Med. Biol.* **32** 121

[22] Sarvas J 1987 *Phys. Med. Biol.* **32** 11

[23] Nenonen J T, Hamalainen M S and Ilmoniemi R J 1994 *Med. Biol. Eng. Comput.* **32** 43

[24] Osama A M and Fuat G U 1993 *IEEE Trans. Magnet.* **29** 1403

[25] Tissari S and Jussi R 2002 *Comput. Meth. Prog. Biomed.* **72** 209